catalysts

MDPI

Article

Role of $SrCO_3$ on Photocatalytic Performance of $SrTiO_3$-$SrCO_3$ Composites

Bíborka Boga [1,2], Norbert Steinfeldt [1], Nikolaos G. Moustakas [1], Tim Peppel [1], Henrik Lund [1], Jabor Rabeah [1], Zsolt Pap [3,4,5], Vasile-Mircea Cristea [2] and Jennifer Strunk [1,*]

1 Leibniz Institute for Catalysis (LIKAT), Albert-Einstein-Str. 29a, 18059 Rostock, Germany
2 Faculty of Chemistry and Chemical Engineering, Babeș-Bolyai University, Arany János Str. 11, 400028 Cluj-Napoca, Romania
3 Institute for Interdisciplinary Research on Bio-Nano-Sciences, Babeș-Bolyai University, Treboniu Laurian Str. 42, 400271 Cluj-Napoca, Romania
4 Institute of Research-Development-Innovation in Applied Natural Sciences, Babeș-Bolyai University, Fântânele Str. 30, 400294 Cluj-Napoca, Romania
5 Department of Applied and Environmental Chemistry, University of Szeged, Rerrich Sqr. 1, 6720 Szeged, Hungary
* Correspondence: jennifer.strunk@catalysis.de

Abstract: Perovskites such as $SrTiO_3$ are interesting for photocatalytic applications due to their structure-related and electronic properties. These properties are influenced by the presence of $SrCO_3$ which is often formed simultaneously during the hydrothermal synthesis of $SrTiO_3$. In this study, $SrTiO_3$-$SrCO_3$ composites with different contents of $SrCO_3$ (5–24 wt%) were synthesized. Their morphological, structural, and optical properties were investigated using complementary methods such as scanning electron microscopy (SEM), X-ray diffraction (XRD), nitrogen sorption, and diffuse reflectance spectroscopy (DRS). Their photocatalytic activity was assessed during the degradation of diclofenac (DCFNa) in aqueous solution and CO_2 photoreduction under Xe lamp irradiation. Improved photocatalytic efficiency in DCFNa degradation was observed for all the studied composites in comparison with $SrTiO_3$, and the highest mineralization efficiency was obtained for the sample with 21 wt% $SrCO_3$ content. The presence of $SrCO_3$ led to an increased concentration of active species, such as $^{\bullet}OH$ radicals. Otherwise, its presence inhibits CH_4 and C_2H_6 production during CO_2 photoreduction compared with pure $SrTiO_3$.

Keywords: strontium titanate; strontium titanate-strontium carbonate heterojunction; strontium carbonate; carbonate anion radical; diclofenac; CO_2 photoreduction

Citation: Boga, B.; Steinfeldt, N.; Moustakas, N.G.; Peppel, T.; Lund, H.; Rabeah, J.; Pap, Z.; Cristea, V.-M.; Strunk, J. Role of $SrCO_3$ on Photocatalytic Performance of $SrTiO_3$-$SrCO_3$ Composites. *Catalysts* **2022**, *12*, 978. https://doi.org/10.3390/catal12090978

Academic Editor: Roberto Fiorenza

Received: 5 August 2022
Accepted: 27 August 2022
Published: 31 August 2022

1. Introduction

Titanium-based materials, such as titania, alkaline earth metal titanates, etc., are considered as suitable candidates for photocatalytic applications [1,2]. Among these, $SrTiO_3$ seems to be a promising candidate given its band-structure [3], considerable catalytic activity, and chemical and thermal stability, and the long lifetime of the photogenerated charge carriers [4]. One unique property of $SrTiO_3$ is directly related to its slightly different conduction band (CB) edge situated at a more negative potential in comparison with anatase (i.e., E_{CB}(anatase): −0.1 V, E_{CB}($SrTiO_3$): −0.3 V vs. NHE at pH = 0 [5]), which has a direct influence on its water splitting ability. Although the CB position of TiO_2 (both anatase and rutile) does not allow efficient H_2 production (from H_2O) unless in the presence of co-catalysts, this limitation is overcome in the case of $SrTiO_3$ [6,7].

Moreover, $SrTiO_3$ is one such photocatalyst which exhibits high activity towards both reduction (Cr^{6+}/Cr^{3+} [8], CO_2/solar fuels [9], H_2O/H_2 [10]), and oxidation (photodegradation of contaminants [11]). $SrTiO_3$ is a well-known ABO_3-type model perovskite with ideal cubic structure (geometric tolerance factor ~1) at room temperature [12], possessing

mixed ionic-covalent bonding properties [13], which confer excellent electronic features. Having a closer look at its unit cell, along the crystallographic axis two different types of alternating atomic planes (SrO and TiO_2) can be distinguished, which exhibit different acid-base and electronic properties [9,14]. Although $SrTiO_3$ exhibits favorable photocatalytic features itself, coupling with noble metals (i.e., Ag [15], Pt [16]) or with semiconductors (i.e., TiO_2 [17], Bi_2S_3 [18]) or insulators (i.e., $SrCO_3$ [19–23]) leads to the enhancement of catalytic activity of such composites given by the manifested synergistic effect [24].

Several methods are reported in the literature for the synthesis of $SrTiO_3$, such as solid-state synthesis [25], solvothermal route [11,26], sol-gel [27], molten salt reaction [28], and electrospinning [29]. Among these, hydrothermal synthesis is one of the most promising not only because of mild reaction conditions and efficient control of crystal growth and morphology [11], but also because of simultaneous (inevitable) formation of $SrCO_3$ (as byproduct), thus resulting in $SrTiO_3$-$SrCO_3$ heterojunctions [30,31]. $SrTiO_3$-$SrCO_3$ is considered as one of the most useful composites for photocatalytic applications, such as NO oxidation [19], CH_4 oxidation [20], H_2 generation (H_2O splitting) [21], degradation of methylene blue [22], and photoelectrochemical CO_2 reduction [23], where the $SrCO_3$ content has considerable importance. The efficiency of $SrTiO_3$-$SrCO_3$ in photocatalytic applications can be explained mainly by the improved charge separation provided by $SrCO_3$, which acts as an electron trap. Since the photogenerated electrons from the CB of $SrTiO_3$ are trapped by $SrCO_3$ (and $SrCO_3$ is not excited given its relatively large band gap), the recombination rate of charge carriers is quite decreased in such n–n type heterojunctions [19].

Dissolution of airborne CO_2 in the reaction mixture [11,32–34], the initial molar ratio between the Sr^{2+}:Ti^{4+} precursors [22], and the carbonate content of the applied base [35,36] are potential factors which can influence the amount of $SrCO_3$ formed during the hydrothermal synthesis of $SrTiO_3$. Furthermore, it should be highlighted that the control of the carbonate content of the alkaline reagent is challenging not only because of its high CO_2 absorptivity, but also because of the uniformity of the carbonate content. Beyond the previously mentioned one-step preparation of $SrTiO_3$-$SrCO_3$ via solvothermal synthesis [20,22], in-situ pyrolysis [19], sol-gel [20], and solid-state methods [20] are also reported in the literature as methods to obtain the mixed material.

In this work, $SrTiO_3$-$SrCO_3$ composites with different $SrCO_3$ contents were synthesized and applied for DCFNa photodegradation and CO_2 photoreduction. Preliminary purification of KOH in association with the conduction of synthesis in Schlenk line technique, excess of Sr^{2+} source, and different Ti^{4+} sources (i.e., anatase vs. P25) were applied, aiming for the control of $SrCO_3$ content of $SrTiO_3$-based catalysts. According to our best knowledge, the combination of preliminary purification of KOH with Schlenk line technique and the application of different Ti^{4+} precursors for the adjustment of $SrCO_3$ content of the $SrTiO_3$-based catalysts have not been reported yet in the scientific literature. It is demonstrated that the presence of $SrCO_3$ increases both the DCFNa degradation and its mineralization. Furthermore, some reasons for the higher activity of $SrTiO_3$-$SrCO_3$ compared with $SrTiO_3$ are discussed.

2. Results and Discussion

2.1. Structure, Morphology, and Textural Properties

The powder XRD patterns of the studied catalysts are presented in Figure 1. The commercially available $SrTiO_3$ (cSTO) was considered as the reference catalyst, showing only reflections of the $SrTiO_3$ phase (ICDD 00-035-0734). The notation used for the hydrothermally synthesized samples is STO_x_SCO, where x represents the $SrCO_3$ content (5, 15, 21 and 24 wt%) of the samples determined via Rietveld analysis based on the recorded XRD patterns. The presence of the cubic phase of $SrTiO_3$ is confirmed in the recorded XRD patterns. The additional reflections identified were assigned to the orthorhombic $SrCO_3$ phase (ICDD 01-084-1778). Considerable differences were revealed in the $SrCO_3$ content of the samples as a function of the applied strategy (Table 1, see detailed description in

the Experimental Section). As was expected, the lowest $SrCO_3$ content (i.e., 5 wt%) was assessed when the alkaline reagent had undergone preliminary purification, and the synthesis was conducted under inert conditions. Furthermore, when 25% excess Sr^{2+} source was introduced into the initial reaction mixture, increased $SrCO_3$ content (i.e., 21 wt%) was determined in the final product. Finally, the usage of P25 (instead of anatase) as the Ti^{4+} source had considerable influence on the $SrCO_3$ content (15 vs. 24 wt% when Ti^{4+} source was anatase vs. P25, respectively). Previous studies highlighted the influence of the crystal structure of the TiO_2 precursor (anatase, rutile, or amorphous) on the hydrothermal crystallization of $SrTiO_3$ [37–39] (given the different stability of the precursors [40]), although without referring to the formation and content of $SrCO_3$.

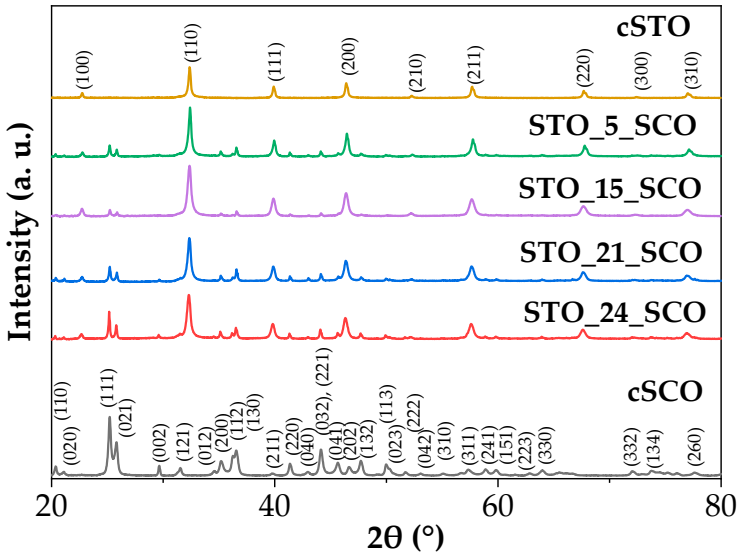

Figure 1. Powder X-ray diffraction pattern of the studied catalysts.

Table 1. Summary of the applied strategy aiming for the control of $SrCO_3$ content and the primary crystallite size (PCS) of components for all tested photocatalysts (STO_x_SCO, x = 5, 15, 21, and 24 wt%).

No.	Samples	Strategy/Observation	PCS_{STO} (nm)	PCS_{SCO} (nm)
1	cSTO	—	28	—
2	STO_5_SCO	Preliminary purification of KOH and Schlenk line technique	18	49
3	STO_15_SCO	Starting synthesis	25	55
4	STO_21_SCO	$r_n(Sr^{2+}:Ti^{4+}) = 1.25$	20	54
5	STO_24_SCO	Modification of Ti^{4+} source	19	57

The content of $SrCO_3$ calculated from the C content (determined by elemental analysis) was in concordance with the results obtained based on Rietveld analysis.

The primary crystallite size (PCS) of components is summarized in Table 1. The PCS of $SrTiO_3$ was in the range of 18–28 nm, whereas much higher values (49–57 nm) were obtained in the case of $SrCO_3$.

According to Figure 2, different $SrCO_3$ content, and more implicitly different synthesis parameters, have only moderate influence on the PCS of $SrTiO_3$ and $SrCO_3$. In each case the PCs of $SrCO_3$ was higher than that of $SrTiO_3$.

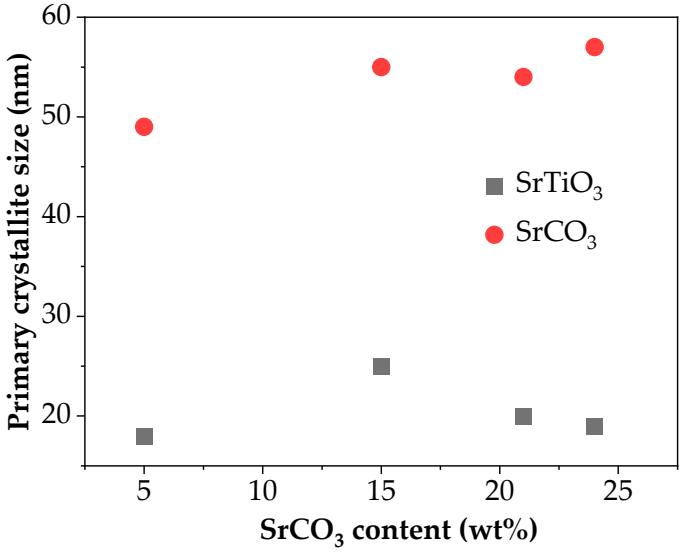

Figure 2. Primary crystallite size (PCS) vs. $SrCO_3$ content of the hydrothermally synthesized samples.

The SEM micrographs of the selected hydrothermally synthesized $SrTiO_3$-based samples, namely STO_15_SCO and STO_24_SCO, are presented in Figure 3. No considerable differences are revealed in the case of the selected STO-based samples regardless of the Ti^{4+} precursor type (P25 or anatase). Two characteristic morphologies were identified, namely nanocubes and microrods (marked with white dotted line). The length of these microrods was situated between 1–1.5 µm, and their width was identified in the 165–400 nm range. The characteristic dimension of the nanocubes varied in the range of 40–80 nm, which is in agreement with the results reported in the literature [4,38].

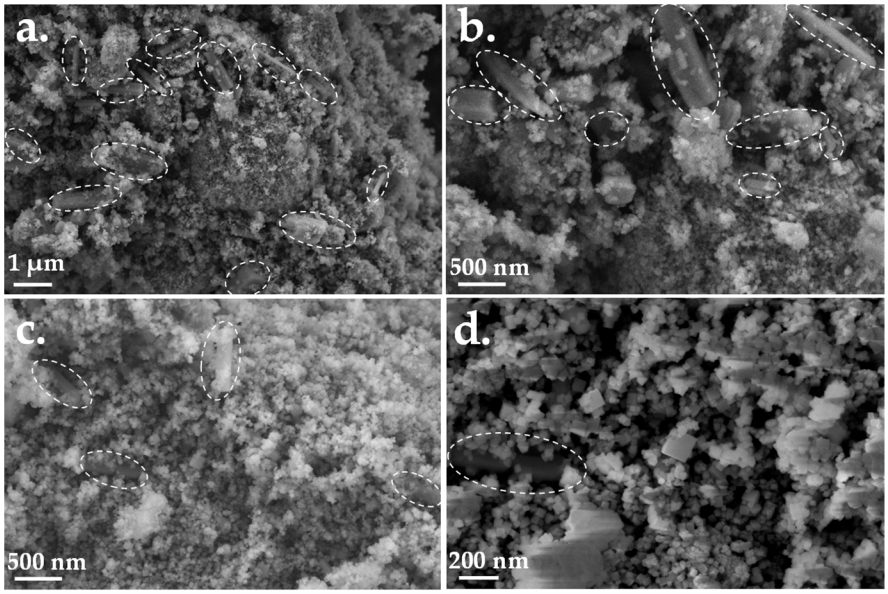

Figure 3. SEM micrographs of STO_15_SCO (**a**,**b**) and STO_24_SCO (**c**,**d**).

The lowest specific surface area (BET-SSA) was assigned to the commercial $SrTiO_3$ (Table 2), because of its spherical morphology, which is characterized by the lowest surface area to volume ratio. Furthermore, relatively low SSA was determined in the case of STO_5_SCO in comparison with the other hydrothermally synthesized samples (i.e., STO_x_SCO, where x: 15, 21, 24). According to Table 2, there is no direct correlation between the SSA and $SrCO_3$ content of the hydrothermally synthesized $SrTiO_3$-based

catalysts, but the presence of higher $SrCO_3$ content seems to enhance the SSA. Similar observations were presented in the work of Marquez-Herrera and coworkers [22].

Table 2. Specific surface area and optical properties of the studied catalysts.

Samples	SSA-BET ($m^2 \cdot g^{-1}$)	ΔE_g (eV)	λ_{thres} (nm)	E_{thres} (eV)
cSTO	15	3.23	374	3.32
STO_5_SCO	16	3.18	371	3.34
STO_15_SCO	45	3.16	378	3.28
STO_21_SCO	33	3.18	379	3.27
STO_24_SCO	41	3.16	377	3.29

Abbreviations: ΔE_g—band gap, λ_{thres} and E_{thres}—wavelength and energy corresponding to the absorption threshold.

2.2. Optical Properties

The absorption spectra of the studied samples were recorded in the UV-Vis range (Figure 4a). As expected, the STO-based samples absorb photons mainly from the UV-range (200–400 nm). The band gap energy values (ΔE_g) were calculated from the Tauc-plot (Figure 4b) considering the appropriate exponent (0.50) for indirect band gap semiconductors [4]. The well-known procedure (i.e., extrapolation of the linear region of the Tauc-plot) was applied, which led to ΔE_g values situated in the range of 3.1–3.2 eV (Table 2). The ΔE_g values determined for commercial and hydrothermally synthesized $SrTiO_3$ are in agreement with the values reported in literature [41]. No considerable shift in the absorption edge can be observed in the case of samples with different $SrCO_3$ content in the recorded range, since $SrCO_3$ absorbs electromagnetic radiation characterized with relatively high energy (4.9 eV [22]), which cannot be resolved within the recorded range. Furthermore, the absorption threshold (λ_{thres}, E_{thres}) of the studied catalysts was determined based on the first derivative reflectance spectra and summarized in Table 2. As was expected, slightly higher values were assigned for the absorption threshold energies in comparison with the ΔE_g.

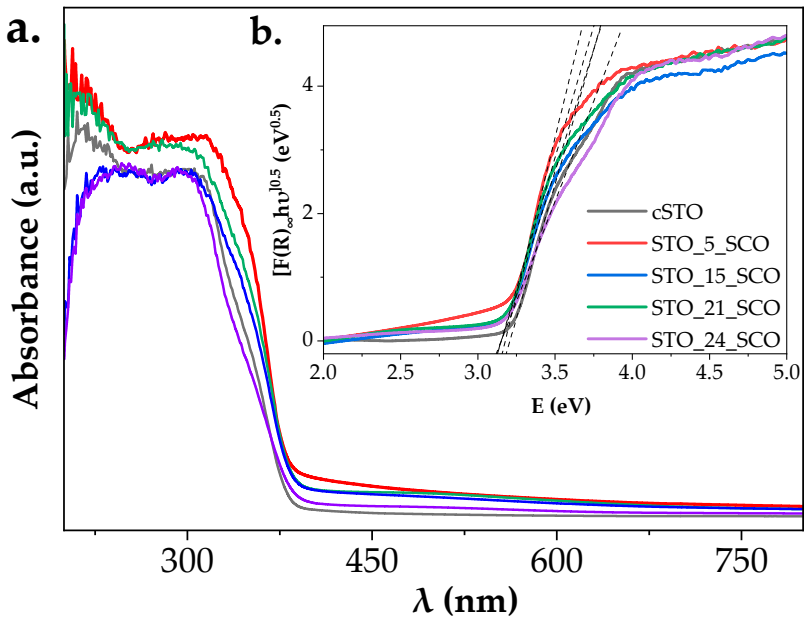

Figure 4. (**a**) UV-Vis spectra of $SrTiO_3$-based catalysts; (**b**) Tauc-plot of the studied $SrTiO_3$-based samples.

2.3. Photocatalytic Results

2.3.1. Photocatalytic Diclofenac Degradation

The photocatalytic activity of the $SrTiO_3$-$SrCO_3$ composites was assessed by the degradation of DCFNa (C_0 = 25 mg·L^{-1}) in aqueous solution under white light irradiation. The degradation curves are presented in Figure 5a. 30 min were allocated for the establishment of adsorption-desorption equilibrium (stirring, dark) before turning on the light. Neglectable DCFNa adsorption can be observed in case of all the $SrTiO_3$-based catalysts after the dark phase, which can be explained by the relatively low differences in SSA (15–45 m^2·g^{-1}). The degradation of DCFNa was almost complete after 1 h irradiation in all studied samples (inclusively the commercial $SrTiO_3$ and $SrTiO_3$-$SrCO_3$ composites). This indicates that the presence of $SrCO_3$ mainly affects the mineralization, i.e., total oxidation of DCFNa. The degradation curve can be described by pseudo first-order kinetics (see Figure S1, Supplementary Material) as previously reported [42]. The fastest DCFNa degradation was achieved for STO_5_SCO and STO_21_SCO. Here, the rate constant was four times higher than that of pure $SrTiO_3$ (cSTO). Beside DCFNa degradation, the effect of $SrCO_3$ content on mineralization was also investigated after 4 h. The mineralization of DCFNa during photolysis was below 3%, which was in agreement with previously reported results [43]. According to Figure 5b, higher mineralization efficiencies (X_{min}) were observed in case of samples containing t$SrCO_3$ phase in comparison with cSTO. Although quite similar mineralization efficiencies were assessed in the cases of STO_5_SCO and STO_15_SCO (~50%), the highest efficiency was reported in the case of STO_21_SCO (62%). Similar optimal $SrCO_3$ content (i.e., 19 wt%) of the $SrTiO_3$-$SrCO_3$ catalyst was determined by Marquez-Herrera during the photodegradation of methylene blue [22].

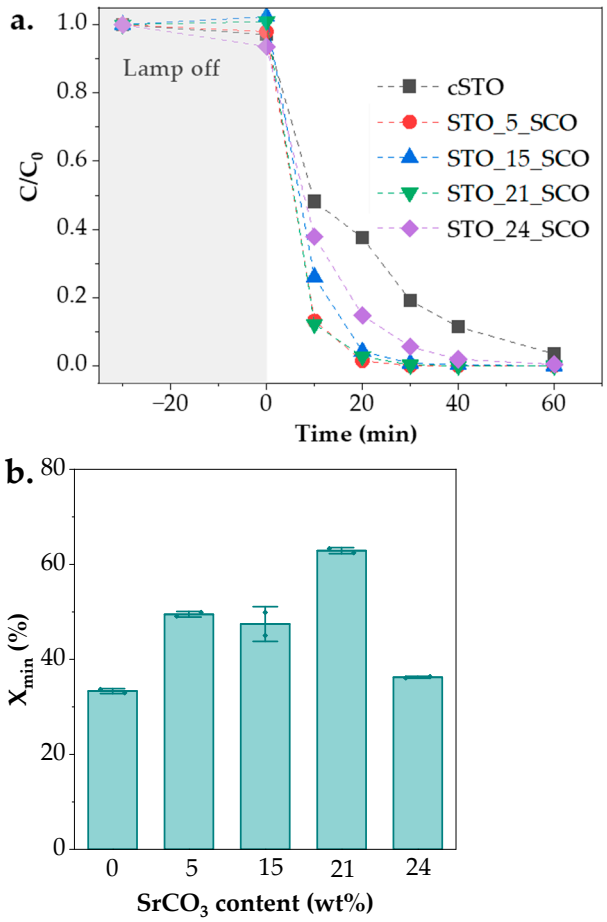

Figure 5. (**a**) The degradation curves of DCFNa and (**b**) the effect of $SrCO_3$ content on DCFNa mineralization after 4 h.

To obtain information about the role of active species (namely h^+, $^\bullet O_2^-$, $^\bullet OH$) in DCFNa degradation, experiments were conducted with the addition of scavengers (ammonium oxalate—AO, 1,4-benzoquinine—PBQ, and isopropanol-IPA) [44] using STO_15_SCO as catalyst (Figure 6). According to Figure 6., the rate of DCFNa degradation only slightly decreased when AO, PBQ, or IPA were added to the reaction mixture, which indicated that none of the active species had considerable influence on the transformation of DCFNa in this case. However, comparing the effects of scavengers, the involvement of $^\bullet OH$ was the most pronounced in comparison with h^+ and $^\bullet O_2^-$.

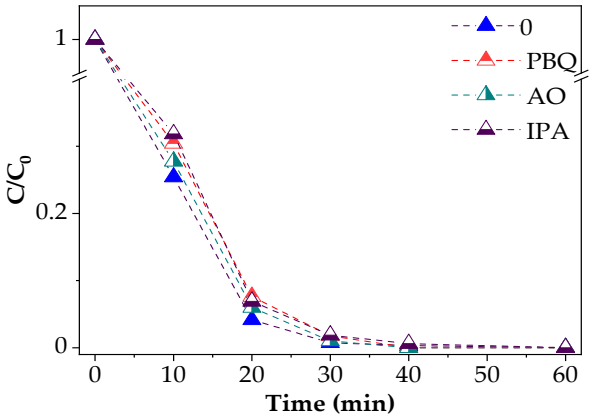

Figure 6. The degradation curves of DCFNa using STO_15_SCO with and without addition of scavengers.

To investigate whether the presence of $SrCO_3$ can influence the amount of reactive $^\bullet OH$ formed during irradiation, the terephthalic acid hydroxylation reaction was carried out using STO_15_SCO and cSTO (Figure 7a). Considering the proportionality between concentration and photoluminescence (PL) intensity, the amount of $^\bullet OH$ was 3.5 times higher in the reaction mixture using STO_15_SCO in comparison with cSTO. Since improved charge separation takes place in $SrTiO_3$-$SrCO_3$ composites [19] (Figure 8), more holes are left over $SrTiO_3$, which may lead to the formation of higher amounts of $^\bullet OH$. However, this is just evidence for better charge separation, and not for the fact that $^\bullet OH$ are the main active species responsible for the photodegradation of DCFNa.

Furthermore, to find out whether beside $^\bullet OH$, further radicals were formed during the photocatalytic reaction, in-situ EPR measurements were conducted with DMPO as a trapping agent using cSTO and STO_15_SCO (Figure 7b). Analyzing the g value (2.007) and the hyperfine splitting constants ($a_N/a_H = 1$), the DMPO/$^\bullet OH$ adduct ($a_N/a_H = 1$ [45]) was identified in the reaction mixture when cSTO and STO_15_SCO were used (Figure 7b). When STO_15_SCO was used, signals of a second radical were additionally observed, which can be attributed to the formation of a DMPO/$CO_3^{\bullet -}$ adduct ($a_N/a_H = 1.37$ [45]). Analyzing the redox potentials of $CO_3^{\bullet -}/CO_3^{2-}$ (1.54 V vs. NHE) and $H_2O/^\bullet OH$ (2.8 V vs. NHE) redox pairs, it is obvious that $CO_3^{\bullet -}$ is a weaker oxidizing agent than $^\bullet OH$ [46]. Even though the carbonate anion radical was detected in only small amounts when $SrTiO_3$-$SrCO_3$ was used (Figure 7b), and it is a thermodynamically weak oxidizing agent, these facts do not exclude its possible involvement in the surface reactions (i.e., it may be a kinetically fast reaction partner). Moreover, the previously presented scavenging experiments performed using STO_15_SCO (i.e., the addition of $^\bullet OH$ scavenger—IPA has reduced effect on the degradation rate, Figure 6) can be possible evidence for the specific role of the carbonate anion radical when $SrTiO_3$-$SrCO_3$ was used.

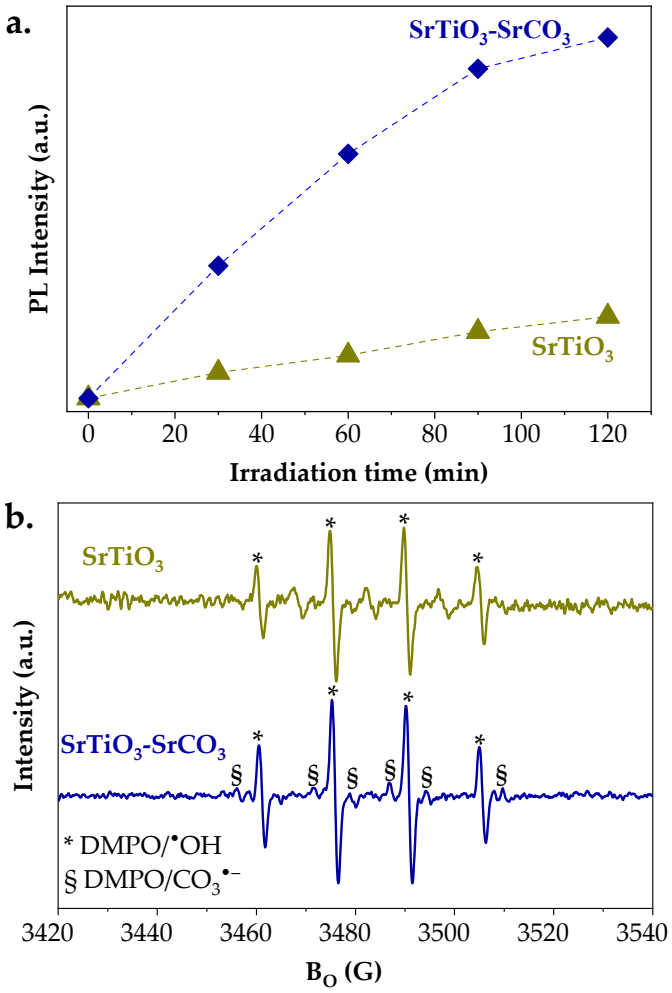

Figure 7. (**a**). Time-dependent terephthalic acid hydroxylation in the cases of cSTO and STO_15_SCO. (**b**). In-situ EPR spectra of the reaction mixture after the addition of DMPO in the presence of cSTO and STO_15_SCO.

According to the scientific literature, the formation of carbonate anion radical can take place (1) through the reaction between hydroxyl radicals and carbonate anions [46], or (2) through the recombination of h^+ by e^- provided from CO_3^{2-} [47]. In the latter case, the recombination of the generated charge carrier might be reduced, and more electrons can react with the dissolved oxygen to form the superoxide radical. Regardless of either of the previously presented mechanisms, the direct involvement of carbonate anions is obvious. To elucidate the formation of carbonate anion radical, first the inorganic carbon content of the final reaction mixture (IC_{final}) was evaluated (Figure S2, Supplementary Material). Although considerably lower IC_{final} was assessed using cSTO ($IC_{final\text{-}cSTO}$ ~ 700 $\mu g \cdot L^{-1}$) in comparison with the STO_x_SCO ($IC_{final\text{-}STO\_x\_SCO}$ > 3 $mg \cdot L^{-1}$), this value is relatively high compared with the IC_{final} using other catalysts (e.g., P25; $IC_{final,\ P25}$ ~ 120 $\mu g \cdot L^{-1}$). The relatively high IC_{final} using $SrTiO_3$-$SrCO_3$ catalysts clearly indicates the dissolution of carbonate into the reaction mixture, given by its moderate solubility in aqueous medium (0.01 g $SrCO_3$/L H_2O) [48], thus the carbonate anions mainly resulted from the catalyst. Moreover, the dependence of IC_{final} (and implicitly the concentration of carbonate anions in the reaction mixture) on the $SrCO_3$ content of the studied samples can be highlighted (Figure S2, Supplementary Material). Second, the Rietveld analysis performed based on the XRD pattern of the spent catalyst (STO_15_SCO, Figure S3, Supplementary Material) also confirmed carbonate dissolution via the decreased $SrCO_3$ content of the catalyst after reaction. In addition to this, the relatively high $IC_{final\text{-}cSTO}$ (compared with $IC_{final\text{-}P25}$)

can be explained considering the dissolution of airborne CO_2 into the reaction mixture, followed by the formation of carbonate layer on the surface of $SrTiO_3$ [49] (PZC($SrTiO_3$): ~8.5–9.5 [50]), and its further dissolution into the reaction mixture.

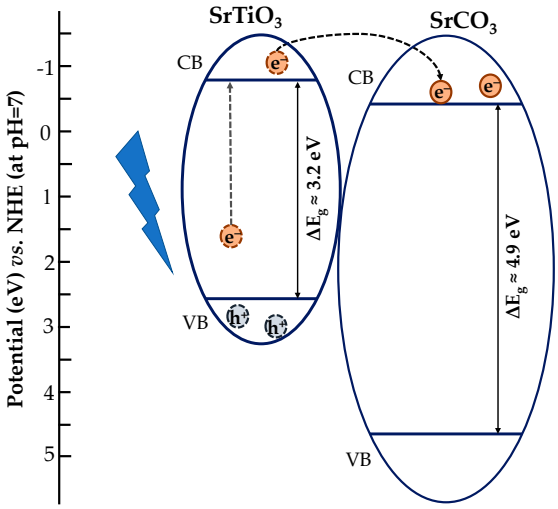

Figure 8. Scheme of the mechanism in $SrTiO_3$-$SrCO_3$ [19,51].

Finally, the reusability of the most efficient catalyst (STO_21_SCO) was tested in three cycles. The transformation of DCFNa was complete after 1 h during the three cycles (Figure S4, Supplementary Material); however, the mineralization of DCFNa did not take place starting from the second cycle. The XRD patterns of the best performing catalyst before the photocatalytic test and after the third cycle are depicted in Figure 9. The deactivation of the catalyst after 4 h might be explained by the adsorption of certain intermediates/products or by the loss of the carbonate phase. This assumption was supported by the observed mass loss of the spent catalyst in the TGA experiments which was obvious higher than that of the fresh catalyst (Figure S5, Supplementary Material).

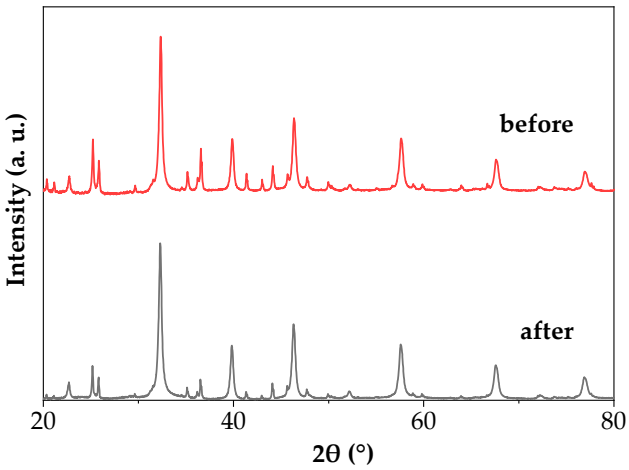

Figure 9. Powder X-ray diffraction pattern of the best performing catalyst before and after the photocatalytic tests (after three cycles).

2.3.2. Photocatalytic CO_2 Reduction Experiments

As the efficiency of $SrTiO_3$ towards both oxidation and reduction is reported in the literature, our curiosity has led us to assess the efficiency of $SrTiO_3$-$SrCO_3$ in a gas-solid photocatalytic CO_2 reduction experiment. Furthermore, a relatively limited number of studies are available aiming for the assessment of $SrTiO_3$-$SrCO_3$ photocatalytic activity

in CO_2 reduction experiments. Although promising selectivity was reported by Li and coworkers towards photocatalytic CO_2-to-CO activity using $SrTiO_3$-$SrCO_3$ [51], Gyulavari and coworkers concluded that the presence of $SrCO_3$ had a negligible influence on the photocatalytic CO_2 reduction activity of $SrTiO_3$- $SrCO_3$ vs. $SrTiO_3$ under the studied experimental conditions [52].

The STO_15_SCO and cSTO samples were evaluated within this section to get an overview on the photocatalytic CO_2 reduction activity of $SrTiO_3$-$SrCO_3$ and $SrTiO_3$ samples. The CO_2 photoreduction step (CRR) was preceded by batch cleaning (BC) to remove the carbon-containing impurities (e.g., precursors and solvents used for synthesis; adsorbed species, such as CO_2 from atmosphere), which can lead to the overestimation of the products resulting from CO_2 photoreduction [53]. In the presence of CO_2 after 6 h of irradiation, the formation of 4.6 ppm and 1.6 ppm of CH_4 could be observed over cSTO and STO_15_SCO, as well as traces of C_2H_6 (Figure 10). In the literature, besides CH_4, the formation of CO is reported during photocatalytic CO_2 reduction experiments over $SrTiO_3$ under different experimental conditions [9,52]. Since the detection limit of the GC employed for the identification of the reaction products is for CO at approximately 20 ppm, the formation of CO cannot be excluded under the selected reaction conditions. Other differences compared with published works may result from the difference in reaction conditions (here gas-solid, no liquid phase).

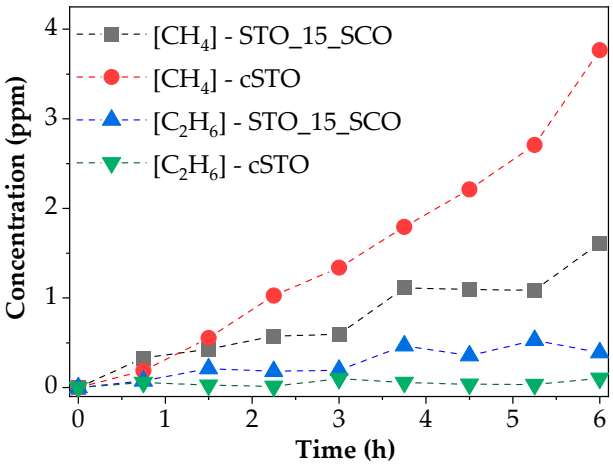

Figure 10. Concentrations of CH_4 and C_2H_6 formed over time in the presence of CO_2 for the hydrothermally synthesized $SrTiO_3$ (STO_15_SCO) and commercial $SrTiO_3$ (cSTO).

In addition to this, the unfavorable effect of the carbonate of studied $SrTiO_3$-based samples (i.e., STO_15_SCO) on CH_4 production can be highlighted (Figure 10). Similar findings were reported by Pougin and coworkers using titania with enhanced surface carbonate vs. "carbonate-free" titania during photocatalytic CO_2 reduction experiments [54]. The role of carbonates as hole traps on the surface of catalysts has been reported in several works, which is not favorable in the case of (photocatalytic) CO_2 reduction reactions [55–57]. Furthermore, the considerable stability of carbonates should also be considered, which inhibits their involvement in further processes [57].

Although low concentration of products was detected under the selected experimental conditions (CH_4: cSTO, 12.6 $ppm \cdot g_{cat}^{-1} \cdot h^{-1}$ in comparison with STO_15_SCO, 5.4 $ppm \cdot g_{cat}^{-1} \cdot h^{-1}$), the role of $SrCO_3$ as a carbon-containing source can be excluded as it does not seem to contribute to the formation products in the presence or absence of CO_2. As CO_2 photoreduction is a multiparametric reaction, further studies are required under different experimental conditions, e.g., different H_2O and/or CO_2 concentrations, light intensity, etc. For a definite proof of the origin of C-containing products, $^{13}CO_2$ reduction can be employed for the best performing photocatalysts [58].

3. Experimental Materials and Methods

3.1. Chemicals

Strontium nitrate ($Sr(NO_3)_2$, ≥99%, Sigma Aldrich, Germany), titanium (IV) oxide—anatase (TiO_2, 99.5%, IoliTec, Heilbronn, Germany), titanium (IV) oxide-P25 (TiO_2, Evonik, Germany), potassium hydroxide (KOH, ≥85%, Sigma Aldrich, Germany), sodium hydroxide (NaOH, 98%, Acros Organics, Morris Plains, NJ, USA), ethanol (C_2H_6O, >99%, Merck, Darmstadt, Germany), ammonium oxalate monohydrate ($(NH_4)_2C_2O_4 \cdot H_2O$, ≥99%, Sigma Aldrich, Germany), p-benzoquinone ($C_6H_4O_2$, >98%, Sigma Aldrich, Germany), isopropanol (C_3H_8O, 99.9%, Merck, Germany), terephthalic acid ($C_8H_6O_4$, >98%, Merck, Germany), 5,5-dimethyl-1-pyrroline-N-oxide ($C_3H_{11}NO$, >98%, Enzo Life Sciences GmbH, Germany). Commercial strontium titanate ($SrTiO_3$, 99.9%, IoliTec, Germany) and strontium carbonate ($SrCO_3$, 99.9%, Sigma Aldrich, Hamburg, Germany) were used as reference catalysts. The chemicals for synthesis and analysis were used without any preliminary purification except for KOH.

3.2. Material Synthesis

The synthesis of $SrTiO_3$-based catalysts with different $SrCO_3$ content (5, 15, 21, 24 wt%) was carried out via hydrothermal treatment (180 °C, 12 h), followed by washing (once with ethanol, three times with distilled water) and drying (80 °C, 12 h). Only the preparation of the reaction mixture is described in detail, because only this step was carried out in a different way in the case of samples with different STO contents.

The "starting" synthesis (STO_15_SCO) involved the addition of Sr^{2+} and Ti^{4+} precursors into 70 mL H_2O in stoichiometric ratio, thus obtaining an initial reaction mixture with 0.083 M $Sr(NO_3)_2$ and anatase (i.e., 1.270 g $Sr(NO_3)_2$, 0.479 g TiO_2). To facilitate the dispersion of anatase, the as-prepared reaction mixture underwent ultrasonication for 3 min. The last steps involved the addition of KOH (thus achieving 8 M in the reaction mixture), and homogenization (30 min).

STO_5_SCO. Although the same initial precursor concentrations were achieved as in the previous case (i.e., 0.083 M $Sr(NO_3)_2$ and TiO_2 (anatase), 8 M KOH), in this case the hydrothermal treatment was conducted at a smaller scale ($V_{autoclave}$ = 47 mL, $V_{reaction\ mixture}$ = 30 mL), due to the complexity of this approach. To assess the influence of scaling-up, the previously presented ''starting" synthesis (STO_15_SCO) was also carried out at this scale. The effect of scaling-up on the morphological, structural, and photocatalytic properties was negligible. The requirements of Schlenk line technique were considered during the synthesis of STO_5_SCO, as presented (i–iv):

(i) 33.663 g KOH was added gradually and dissolved in 50 g degassed water under Ar atmosphere, thus obtaining a 14 M KOH solution. The removal of K_2CO_3 from the concentrated KOH solution was performed considering the method reported by P. Sipos and coworkers [59]. More precisely, 50 mg CaO was added to the concentrated KOH solution and stirred overnight under inert conditions. The separation of the clear KOH solution (C_{KOH}~14 M, solution A) from the formed $CaCO_3$ was realized by applying the cannula method.

(ii) 0.653 g $Sr(NO_3)_2$ was dissolved in 12 g H_2O in a Schlenk flask (2.57×10^{-4} M) under Ar atmosphere (solution B).

(iii) The autoclave ($V_{autoclave}$ = 47 mL) was purged with Argon, followed by the addition of 0.205 g anatase, followed by its immediate coverage.

(iv) 10.544 g solution B was withdrawn with a syringe and transferred to the autoclave

(v) 33.465 g solution A was transferred to the autoclave in a similar manner to solution A. The reaction mixture was stirred for 30 min, followed by hydrothermal crystallization.

The synthesis of STO_21_SCO was performed as the "starting" synthesis (i.e., STO_15_SCO) with the exception that in this case the initial Sr^{2+}:Ti^{4+} molar ratio was 1.25:1.

The difference in the case of STO_24_SCO (vs. "starting" synthesis) was related to the usage of P25 as a Ti^{4+} precursor (instead of pure anatase).

3.3. Characterization

The structural and morphological features of the catalyst were assessed via **scanning electron microscopy (SEM)**. The SEM micrographs were recorded using a Merlin VP compact device (Zeiss, Oberkochen, Germany).

The **X-ray diffraction (XRD)** patterns were recorded on an Xpert Pro diffractometer (Panalytical, Almelo, the Netherlands) using $CuK_{\alpha 1}K_{\alpha 2}$ radiation (λ_1 = 0.15406 nm, λ_1 = 0.15443 nm). The primary crystallite size (τ) was calculated via Scherrer equation considering the as-called shape factor (K = 0.90 used for spherical crystallites), X-ray wavelength (λ), full width at half maximum (β), and peak position (θ) [60]:

$$\tau = \frac{K \cdot \lambda}{\beta \cdot \cos\theta} \quad (1)$$

The phase composition was determined via Rietveld analysis using HighScore Plus.

The **UV-Vis spectra** of the solid catalysts were recorded via a Lambda 650 spectrophotometer (Perkin Elmer, Waltham, MA, USA). The band gap values were determined based on the Tauc-plot.

NOVAtouch (Quantachrome Instruments, Boynton Beach, FL, USA) was used for the collection of the **nitrogen sorption data** at 77 K. The (BET) multipoint method was considered for the determination of specific surface area (p/p_0: 0.05–0.3). The pre-treatment of the samples was performed via heating at 350 °C under vacuum for 5 h.

Thermogravimetric analysis (TGA) of the catalyst was performed via a Netzsch STA 449 F3 Jupiter device (Selb, Germany) in the temperature range of 25–600 °C in air atmosphere.

The photodegradation experiments took place in a double jacket glass cylindrical batch photoreactor (V = ~120 mL, Hassa labor, Lübeck, Germany). The suspension was irradiated with a Xe arc lamp (300 W) equipped with a reflector system (LOT Quantum Design, Darmstadt, Germany). The irradiation of the reaction mixture was carried out from the top, where the distance between the reactor and reflector system was 6 cm. The light intensity inside of the reactor (at 8 cm distance from the reflector system) was 625 $mW \cdot cm^{-2}$. The photocatalytic experiments were conducted at a constant temperature (25 °C). The mass-transfer was facilitated via assuring continuous synthetic air flow (15 $mL \cdot min^{-1}$) and stirring (500 rpm). 40 mg $SrTiO_3$-based catalyst was suspended in 40 mL aqueous solution of diclofenac (C_0 = 25 $mg \cdot L^{-1}$), followed by stirring for 30 min under air flow prior irradiation. The DCFNa transformation was followed by **high-performance liquid chromatography** (HPLC, Agilent Technologies, 1260 Infinity Series, Santa Clara, CA, USA). The mineralization efficiency was assessed after 4 h by evaluating the total organic carbon content (TOC) of the filtered (20 μm) reaction mixture. The dissolved carbonate content from the $SrTiO_3$-based catalyst was quantified via the inorganic carbon content of the reaction mixture (IC) using a **TOC analyzer** (multi N/C, 3100, Analytik Jena, Jena, Germany).

The same experimental conditions were applied during the **scavenging experiments** as during the degradation experiments, using ammonium oxalate (AO), p-benzoquinone (PBQ), and isopropanol (IPA). The initial concentration of scavengers in the reaction mixture was 393 μM (AO, PBQ) and 1.57 mM (IPA).

The **trapping of the hydroxyl radicals** in the final reaction mixture was carried out according to the method described by Marschall and coworkers [61]. In this step, 40 mg catalyst was dispersed in 40 mL NaOH aqueous solution (2×10^{-3} M) with 5×10^{-4} M terephthalic acid. Although similar conditions were maintained as described previously at the photodegradation section, the duration of this radical-trapping experiment was 2 h. 4 mL samples were withdrawn (at 30, 60, 90, 120 min) and filtered. The formation of hydroxylated terephthalic acid compound (TA-OH) was assessed by setting 318 nm as the excitation wavelength and recording the photoluminescence spectra in the range of 350–600 nm via a Varian Cary Eclipse Fluorescence Spectrometer (Agilent Technologies, Mulgrave, Australia).

The identification of the active species in the reaction mixture was performed via **in-situ electron paramagnetic resonance (in-situ EPR)** measurements using 5,5-dimethyl−1-pyrroline-N-oxide (DMPO) as a trapping agent. X-band-EPR spectra were recorded via a Bruker EMX CW-micro EPR spectrometer (Rheinstetten, Germany). The reaction mixture was irradiated for 10 min prior to the addition of the trapping agent (10 µL DMPO). The g value was calculated according to Equation (2), considering the frequency (v), the resonance filed (B_0), Bohr magneton ($\beta = 9.27 \times 10^{-27}$ J·mT^{-1}) and Planck constant ($h = 6.626 \times 10^{-34}$ J·s):

$$g = \frac{h \cdot v}{\beta \cdot B_0} \quad (2)$$

The **photocatalytic CO_2 reduction activity** of the selected $SrTiO_3$-based samples was assessed in a high-purity gas phase photoreactor system described in detail by Mei et al. [62]. The main parts of this system include the reaction chamber, a Hg/Xe lamp (200 W, light intensity: 200 mW·cm^{-2}, Newport-Oriel, Stratford, CT, USA), mass flow controllers, water saturators to humidify the inlet gases, a gas chromatograph (Tracera-2010, Shimadzu; Berlin, Germany), and a vacuum pump. The high purity flow of He (99.9999%) and 1.5 CO_2 (99.9995%)/He (99.9999%) were controlled by the mass flow controllers. The experiments were performed in batch mode, consisting of a batch cleaning (0.6 vol% H_2O/He) and CO_2 reduction experiments (1.5 vol% CO_2/He). According to the Antoine equation, the adjustment of initial H_2O vapor concentration in the reactor was realized by controlling the initial pressure (1500 mbar) and the temperature in the water saturators (278 K). The batch-mode experiments were preceded by flow measurements (in other words, the system was purged either by humified He or by CO_2/He) until the O_2 was removed from the system. The next step was related to the filling of the reactor with the appropriate gas mixture, reaching 1500 mbar as initial pressure. Gaseous samples were withdrawn in 45 min, which induced a pressure drop after each sample withdrawal. The detection and analysis of the products (CH_4, C_2H_6, CO, H_2, and other products) was carried out by the Shimadzu Tracera GC equipped with a barrier ionization discharge (BID) and flame ionization (FID) detectors.

4. Conclusions

This study shows different methods which can be applied to adjust the $SrCO_3$ content of hydrothermally synthesized $SrTiO_3$. Similar primary crystallite size (of STO: 18–28 nm), band gap energy (3.16–3.23 eV) and specific surface area (15–45 m^2·g^{-1}) values were determined in the case of all studied $SrTiO_3$-based samples with 5, 15, 21, or 24 wt% $SrCO_3$ content.

Furthermore, the photocatalytic performance of $SrTiO_3$-$SrCO_3$ catalysts was assessed in both oxidation (diclofenac mineralization) and reduction processes (CO_2 reduction).

Improved diclofenac mineralization (after 4 h) was determined in the cases of all $SrTiO_3$-$SrCO_3$ catalysts (vs. $SrTiO_3$) with an optimal $SrCO_3$ content of 21 wt% ($X_{mineralization}$ = 62%). The enhanced mineralization of diclofenac using $SrTiO_3$-$SrCO_3$ (*vs.* $SrTiO_3$) may be explained by (1) the involvement of $CO_3^{\bullet-}$ (in-situ EPR), (2) better charge separation (and implicitly higher concentration of formed $^{\bullet}OH$), and (3) favorable morpho-structural and textural properties (i.e., higher surface area). Finally, although higher CO_2 reduction activity was assessed for $SrTiO_3$ in comparison with $SrTiO_3$-$SrCO_3$, further investigations are required to clarify the involvement of $SrCO_3$.

Supplementary Materials: The following supporting information can be downloaded at: https://www.mdpi.com/article/10.3390/catal12090978/s1. Table S1: The first-order reaction rate constants (k) in association with the determination coefficients (R^2); Figure S1: Plot of $\ln(C_0/C)$ vs. time; Figure S2: The inorganic carbon content of the final reaction mixture (IC_{final}) vs $SrCO_3$ content of the fresh catalyst; Figure S3: The XRD pattern of the catalyst before and after the 4 h photodegradation test; Figure S4: The transformation of DCFNa over 3 cycles using STO_21_SCO; Figure S5: TGA thermogram for the best performing catalyst (STO_21_SCO) before and after degradation of DCFNa.

Author Contributions: Conceptualization, B.B., N.S. and J.S.; formal analysis, B.B., N.G.M. and H.L.; funding acquisition, N.S. and J.S.; investigation, B.B., N.G.M., T.P., H.L. and J.R.; methodology, B.B., N.S., T.P. and J.S.; supervision, N.S. and J.S.; validation, N.S., T.P., H.L. and J.S.; writing—original draft, B.B., N.S. and J.S.; writing—review and editing, B.B., N.S., N.G.M., T.P., H.L., J.R., Z.P., V.-M.C. and J.S. All authors have read and agreed to the published version of the manuscript.

Funding: This research was funded by German Federal Environmental Foundation (Deustche Bundesstiftung Umwelt), registration number 30021/950.

Data Availability Statement: Data is contained within the article or Supplementary Material.

Acknowledgments: Bíborka Boga gratefully acknowledges the scholarship provided by German Federal Environmental Foundation (Deutsche Bundesstiftung Umwelt), Márton Áron Szakkollégium (funded by the Hungarian Ministry of Economic and Foreign Affairs), and Forerunner Federation. In addition, the authors would like to thank Michael Sebek and Phong Dam for their contribution to this work. Furthermore, special thanks to the Analytical Department of LIKAT, namely to Astrid Lehmann (EA) and Felix Lorenz (BET).

Conflicts of Interest: The authors declare no conflict of interest.

References

1. Solís, R.R.; Bedia, J.; Rodríguez, J.J.; Belver, C. A review on alkaline earth metal titanates for applications in photocatalytic water purification. *Chem. Eng. J.* **2021**, *409*, 128110. [CrossRef]
2. Nasr, M.; Eid, C.; Habchi, R.; Miele, P.; Bechelany, M. Recent Progress on Titanium Dioxide Nanomaterials for Photocatalytic Applications. *ChemSusChem* **2018**, *11*, 3023–3047. [CrossRef] [PubMed]
3. Fujisawa, J.-I.; Eda, T.; Hanaya, M. Comparative study of conduction-band and valence-band edges of TiO_2, $SrTiO_3$, and $BaTiO_3$ by ionization potential measurements. *Chem. Phys. Lett.* **2017**, *685*, 23–26. [CrossRef]
4. Wu, G.; Li, P.; Xu, D.; Luo, B.; Hong, Y.; Shi, W.; Liu, C. Hydrothermal synthesis and visible-light-driven photocatalytic degradation for tetracycline of Mn-doped $SrTiO_3$ nanocubes. *Appl. Surf. Sci.* **2015**, *333*, 39–47. [CrossRef]
5. Chou, H.-L.; Hwang, B.-J.; Sun, C.-L. Catalysis in Fuel Cells and Hydrogen Production. In *New and Future Developments in Catalysis: Batteries, Hydrogen Storage and Fuel Cells*; Suib, S.L., Ed.; Elsevier: Amsterdam, The Netherlands, 2013; pp. 219–263.
6. Kudo, A.; Miseki, Y. Heterogeneous photocatalyst materials for water splitting. *Chem. Soc. Rev.* **2009**, *38*, 253–278. [CrossRef]
7. Canu, G.; Buscaglia, V. Hydrothermal synthesis of strontium titanate: Thermodynamic considerations, morphology control and crystallisation mechanisms. *CrystEngComm* **2017**, *19*, 3867–3891. [CrossRef]
8. Yang, D.; Sun, Y.; Tong, Z.; Nan, Y.; Jiang, Z. Fabrication of bimodal-pore $SrTiO_3$ microspheres with excellent photocatalytic performance for Cr(VI) reduction under simulated sunlight. *J. Hazard. Mater.* **2016**, *312*, 45–54. [CrossRef]
9. Luo, C.; Zhao, J.; Li, Y.; Zhao, W.; Zeng, Y.; Wang, C. Photocatalytic CO_2 reduction over $SrTiO_3$: Correlation between surface structure and activity. *Appl. Surf. Sci.* **2018**, *447*, 627–635. [CrossRef]
10. Sakata, Y.; Miyoshi, Y.; Maeda, T.; Ishikiriyama, K.; Yamazaki, Y.; Imamura, H.; Ham, Y.; Hisatomi, T.; Kubota, J.; Yamakata, A.; et al. Photocatalytic property of metal ion added $SrTiO_3$ to overall H_2O splitting. *Appl. Catal. A Gen.* **2016**, *521*, 227–232. [CrossRef]
11. Huang, S.-T.; Lee, W.W.; Chang, J.-L.; Huang, W.-S.; Chou, S.-Y.; Chen, C.-C. Hydrothermal synthesis of $SrTiO_3$ nanocubes: Characterization, photocatalytic activities, and degradation pathway. *J. Taiwan Inst. Chem. Eng.* **2014**, *45*, 1927–1936. [CrossRef]
12. Fan, Z.; Sun, K.; Wang, J. Perovskites for photovoltaics: A combined review of organic–inorganic halide perovskites and ferroelectric oxide perovskites. *J. Mater. Chem. A* **2015**, *3*, 18809–18828. [CrossRef]
13. Ricci, D.; Bano, G.; Pacchioni, G.; Illas, F. Electronic structure of a neutral oxygen vacancy in $SrTiO_3$. *Phys. Rev. B* **2003**, *68*, 224105. [CrossRef]
14. Raisch, C.; Chassé, T.; Langheinrich, C.; Chassé, A. Preparation and investigation of the A-site and B-site terminated $SrTiO_3$(001) surface: A combined experimental and theoretical x-ray photoelectron diffraction study. *J. Appl. Phys.* **2012**, *112*, 073505. [CrossRef]
15. Shao, K.; Wang, Y.; Iqbal, M.; Lin, L.; Wang, K.; Zhang, X.; He, M.; He, T. Modification of Ag nanoparticles on the surface of $SrTiO_3$ particles and resultant influence on photoreduction of CO_2. *Appl. Surf. Sci.* **2018**, *434*, 717–724. [CrossRef]
16. Wu, X.; Wang, C.; Wei, Y.; Xiong, J.; Zhao, Y.; Zhao, Z.; Liu, J.; Li, J. Multifunctional photocatalysts of Pt-decorated 3DOM perovskite-type $SrTiO_3$ with enhanced CO_2 adsorption and photoelectron enrichment for selective CO_2 reduction with H_2O to CH_4. *J. Catal.* **2019**, *377*, 309–321. [CrossRef]
17. Lv, X.; Lam, F.L.-Y.; Hu, X. Developing $SrTiO_3/TiO_2$ heterostructure nanotube array for photocatalytic fuel cells with improved efficiency and elucidating the effects of organic substrates. *Chem. Eng. J.* **2022**, *427*, 131602. [CrossRef]
18. Ganapathy, M.; Hsu, Y.; Thomas, J.; Chen, L.-Y.; Chang, C.-T.; Alagan, V. Preparation of $SrTiO_3/Bi_2S_3$ heterojunction for efficient photocatalytic hydrogen production. *Energy Fuels* **2021**, *35*, 14995–15004. [CrossRef]
19. Jin, S.; Dong, G.; Luo, J.; Ma, F.; Wang, C. Improved photocatalytic NO removal activity of $SrTiO_3$ by using $SrCO_3$ as a new co-catalyst. *Appl. Catal. B Environ.* **2018**, *227*, 24–34. [CrossRef]

20. Pan, X.; Chen, X.; Yi, Z. Photocatalytic oxidation of methane over $SrCO_3$ decorated $SrTiO_3$ nanocatalysts via a synergistic effect. *Phys. Chem. Chem. Phys.* **2016**, *18*, 31400–31409. [CrossRef]
21. Deng, Y.; Shu, S.; Fang, N.; Wang, R.; Chu, Y.; Liu, Z.; Cen, W. One-pot synthesis of $SrTiO_3$-$SrCO_3$ heterojunction with strong interfacial electronic interaction as a novel photocatalyst for water splitting to generate H_2. *Chin. Chem. Lett.* **2022**, *in press*. [CrossRef]
22. Márquez-Herrera, A.; Ovando-Medina, V.M.; Castillo-Reyes, B.E.; Melendez-Lira, M.; Zapata-Torres, M.; Saldana, N. A novel synthesis of $SrCO_3$–$SrTiO_3$ nanocomposites with high photocatalytic activity. *J. Nanopart. Res.* **2014**, *16*, 2804. [CrossRef]
23. Arai, T.; Sato, S.; Kajino, T.; Morikawa, T. Solar CO_2 reduction using H_2O by a semiconductor/metal-complex hybrid photocatalyst: Enhanced efficiency and demonstration of a wireless system using $SrTiO_3$ photoanodes. *Energy Environ. Sci.* **2013**, *6*, 1274–1282. [CrossRef]
24. Ali, K.; Bahadur, A.; Jabbar, A.; Iqbal, S.; Bashir, M.I. Synthesis, structural, dielectric and magnetic properties of $CuFe_2O_4/MnO_2$ nanocomposite. *J. Magn. Magn. Mater.* **2017**, *434*, 30–36. [CrossRef]
25. Liu, Y.; Xie, L.; Li, Y.; Yang, R.; Qu, J.; Li, Y.; Li, X. Synthesis and high photocatalytic hydrogen production of $SrTiO_3$ nanoparticles from water splitting under UV irradiation. *J. Power Sources* **2008**, *183*, 701–707. [CrossRef]
26. Zhang, S.; Liu, J.; Han, Y.; Chen, B.; Li, X. Formation mechanisms of $SrTiO_3$ nanoparticles under hydrothermal conditions. *Mater. Sci. Eng. B* **2004**, *110*, 11–17. [CrossRef]
27. Chen, L.; Zhang, S.; Wang, L.; Xue, D.; Yin, S. Preparation and photocatalytic properties of strontium titanate powders via sol–gel process. *J. Cryst. Growth* **2009**, *311*, 746–748. [CrossRef]
28. Wang, T.X.; Shuang, Z.L.; Jun, C. Molten salt synthesis of $SrTiO_3$ nanocrystals using nanocrystalline TiO_2 as a precursor. *Powder Technol.* **2011**, *205*, 289–291. [CrossRef]
29. Hou, D.; Hu, X.; Ho, W.; Hu, P.; Huang, Y. Facile fabrication of porous Cr-doped $SrTiO_3$ nanotubes by electrospinning and their enhanced visible-light-driven photocatalytic properties. *J. Mater. Chem. A* **2015**, *3*, 3935–3943. [CrossRef]
30. Skoog, D.A.; West, D.M.; Holler, F.J.; Crouch, S.R. *Fundamentals of Analytical Chemistry*; Thomson Brooks/Cole: Belmont, MA, USA, 2004.
31. Phoon, B.L.; Lai, C.W.; Juan, J.C.; Show, P.; Chen, W. A review of synthesis and morphology of $SrTiO_3$ for energy and other applications. *Int. J. Energy Res.* **2019**, *43*, 5151–5174. [CrossRef]
32. Lim, P.F.; Leong, K.H.; Sim, L.C.; Oh, W.-D.; Chin, Y.H.; Saravanan, P.; Dai, C. Mechanism insight of dual synergistic effects of plasmonic Pd-$SrTiO_3$ for enhanced solar energy photocatalysis. *Appl. Phys. A* **2020**, *126*, 550. [CrossRef]
33. Grabowska, E.; Marchelek, M.; Klimczuk, T.; Lisowski, W.; Zaleska-Medynskaa, A. $TiO_2/SrTiO_3$ and $SrTiO_3$ microspheres decorated with Rh, Ru or Pt nanoparticles: Highly UV–vis responsible photoactivity and mechanism. *J. Catal.* **2017**, *350*, 159–173. [CrossRef]
34. Marchelek, M.; Grabowska, E.; Klimczuk, T.; Lisowski, W.; Giamello, E.; Zaleska-Medynska, A. Studies on novel BiyXz-$TiO_2/SrTiO_3$ composites: Surface properties and visible light-driven photoactivity. *Appl. Surf. Sci.* **2018**, *435*, 1174–1186. [CrossRef]
35. Lencka, M.M.; Riman, R.E. Hydrothermal synthesis of perovskite materials: Thermodynamic modeling and experimental verification. *Ferroelectrics* **1994**, *151*, 159–164. [CrossRef]
36. Kalyani, V.; Vasile, B.S.; Ianculescu, A.; Testino, A.; Carino, A.; Buscaglia, M.T.; Buscaglia, V.; Nanni, P. Hydrothermal Synthesis of $SrTiO_3$: Role of Interfaces. *Cryst. Growth Des.* **2015**, *15*, 5712–5725. [CrossRef]
37. Zhang, Q.; Li, Y.; Ren, Z.; Ahmad, Z.; Li, X.; Han, G. Synthesis of porous $CaTiO_3$ nanotubes with tunable hollow structures via single-nozzle electrospinning. *Mater. Lett.* **2015**, *152*, 82–85. [CrossRef]
38. Jiang, D.; Sun, X.; Wu, X.; Shi, L.; Du, F. Hydrothermal synthesis of single-crystal Cr-doped $SrTiO_3$ for efficient visible-light responsive photocatalytic hydrogen evolution. *Mater. Res. Express* **2019**, *7*, 015047. [CrossRef]
39. Ramos, B.; Ookawara, S.; Matsushita, Y.; Yoshikawa, S. Low-cost polymeric photocatalytic microreactors: Catalyst deposition and performance for phenol degradation. *J. Environ. Chem. Eng.* **2014**, *2*, 1487–1494. [CrossRef]
40. Kutty, T.; Vivekanandan, R.; Murugaraj, P. Precipitation of rutile and anatase (Tio_{12}) fine powders and their conversion to $MTiO_3$ (M = Ba, Sr, Ca) by the hydrothermal method. *Mater. Chem. Phys.* **1988**, *19*, 533–546. [CrossRef]
41. Van Benthem, K.; Elsässer, C.; French, R.H. Bulk electronic structure of $SrTiO_3$: Experiment and theory. *J. Appl. Phys.* **2001**, *90*, 6156–6164. [CrossRef]
42. Zhang, N.; Li, J.M.; Liu, G.G.; Chen, X.L.; Jiang, K. Photodegradation of diclofenac in aqueous solution by simulated sunlight irradiation: Kinetics, thermodynamics and pathways. *Water Sci. Technol.* **2017**, *75*, 2163–2170. [CrossRef]
43. Yamamoto, H.; Nakamura, Y.; Moriguchi, S.; Nakamura, Y.; Honda, Y.; Tamura, I.; Hirata, Y.; Hayashi, A.; Sekizawa, J. Persistence and partitioning of eight selected pharmaceuticals in the aquatic environment: Laboratory photolysis, biodegradation, and sorption experiments. *Water Res.* **2009**, *43*, 351–362. [CrossRef]
44. Vu, V.T.; Bartling, S.; Peppel, T.; Lund, H.; Kreyenschulte, C.; Rabeah, J.; Moustakas, N.G.; Surkus, A.-E.; Ta, H.D.; Steinfeldt, N. Enhanced photocatalytic performance of polymeric carbon nitride through combination of iron loading and hydrogen peroxide treatment. *Colloids Surfaces A Physicochem. Eng. Asp.* **2020**, *589*, 124383. [CrossRef]
45. Villamena, F.A. *EPR Spin Trapping, in Reactive Species Detection in Biology—From Fluorescence to Electron Paramagnetic Resonance Spectroscopy*; Elsevier: Amesterdam, The Netherlands, 2017; pp. 163–202.

46. Vione, D.; Khanra, S.; Man, S.C.; Maddigapu, P.R.; Das, R.; Arsene, C.; Olariu, R.-I.; Maurino, V.; Minero, C. Inhibition vs. enhancement of the nitrate-induced phototransformation of organic substrates by the •OH scavengers bicarbonate and carbonate. *Water Res.* **2009**, *43*, 4718–4728. [CrossRef]
47. Chandrasekaran, K.; Thomas, J. Photochemical reduction of carbonate to formaldehyde on TiO_2 powder. *Chem. Phys. Lett.* **1983**, *99*, 7–10. [CrossRef]
48. Bhatt, C.R.; Jain, J.C.; Edenborn, H.M.; McIntyre, D.L. Mineral carbonate dissolution with increasing CO_2 pressure measured by underwater laser induced breakdown spectroscopy and its application in carbon sequestration. *Talanta* **2019**, *205*, 120170. [CrossRef]
49. Staykov, A.; Fukumori, S.; Yoshizawa, K.; Sato, K.; Ishihara, T.; Kilnerad, J. Interaction of SrO-terminated $SrTiO_3$ surface with oxygen, carbon dioxide, and water. *J. Mater. Chem. A* **2018**, *6*, 22662–22672. [CrossRef]
50. Kosmulski, M. pH-dependent surface charging and points of zero charge. IV. Update and new approach. *J. Colloid Interface Sci.* **2009**, *337*, 439–448. [CrossRef]
51. Li, Z.; Zheng, P.; Zhang, W.; Gong, S.; Zhu, L.; Xu, J.; Rao, F.; Xie, X.; Zhu, G. Constructing $SrCO_3/SrTiO_3$ nanocomposites with highly selective photocatalytic CO_2-to-CO reduction. *Colloids Surf. A Physicochem. Eng. Asp.* **2022**, *650*, 129686. [CrossRef]
52. Gyulavári, T.; Dusnoki, D.; Márta, V.; Yadav, M.; Abedi, M.; Sápi, A.; Kukovecz, Á.; Kónya, Z.; Pap, Z. Dependence of Photocatalytic Activity on the Morphology of Strontium Titanates. *Catalysts* **2022**, *12*, 523. [CrossRef]
53. Handoko, C.T.; Moustakas, N.G.; Peppel, T.; Springer, A.; Oropeza, F.E.; Huda, A.; Bustan, M.D.; Bambang, Y.; Gulo, F.; Strunk, J. Characterization and effect of Ag (0) vs. Ag (I) species and their localized plasmon resonance on photochemically inactive TiO_2. *Catalysts* **2019**, *9*, 323. [CrossRef]
54. Pougin, A.; Dilla, M.; Strunk, J. Identification and exclusion of intermediates of photocatalytic CO_2 reduction on TiO_2 under conditions of highest purity. *Phys. Chem. Chem. Phys.* **2016**, *18*, 10809–10817. [CrossRef]
55. Dimitrijevic, N.M.; Vijayan, B.K.; Poluektov, O.G.; Rajh, T.; Gray, K.A.; He, H.; Zapol, P. Role of water and carbonates in photocatalytic transformation of CO_2 to CH_4 on titania. *J. Am. Chem. Soc.* **2011**, *133*, 3964–3971. [CrossRef] [PubMed]
56. Habisreutinger, S.N.; Schmidt-Mende, L.; Stolarczyk, J.K. Photocatalytic reduction of CO_2 on TiO_2 and other semiconductors. *Angew. Chem. Int. Ed.* **2013**, *52*, 7372–7408. [CrossRef] [PubMed]
57. Strunk, J. Requirements for efficient metal oxide photocatalysts for CO_2 reduction. In *Metal Oxides in Energy Technologies*; Wu, Y., Ed.; Elsevier: Amsterdam, The Netherlands, 2018; pp. 275–301.
58. Moustakas, N.G. Strategic design and evaluation of metal oxides for photocatalytic CO_2 reduction. In *Materials Science in Photocatalysis*; García-López, E.I., Palmisano, L., Eds.; Elsevier: Amsterdam, The Netherlands, 2021; pp. 255–265.
59. Sipos, P.; May, P.M.; Hefter, G.T. Carbonate removal from concentrated hydroxide solutions. *Analyst* **2000**, *125*, 955–958. [CrossRef]
60. Monshi, A.; Foroughi, M.R.; Monshi, M.R. Modified Scherrer Equation to Estimate More Accurately Nano-Crystallite Size Using XRD. *World J. Nano Sci. Eng.* **2012**, *02*, 154–160. [CrossRef]
61. Marschall, R.; Mukherji, A.; Tanksale, A.; Sun, C.; Smith, S.C.; Wang, L.; Lu, M. Preparation of new sulfur-doped and sulfur/nitrogen co-doped $CsTaWO_6$ photocatalysts for hydrogen production from water under visible light. *J. Mater. Chem.* **2011**, *21*, 8871–8879. [CrossRef]
62. Mei, B.; Pougin, A.; Strunk, J. Influence of photodeposited gold nanoparticles on the photocatalytic activity of titanate species in the reduction of CO_2 to hydrocarbons. *J. Catal.* **2013**, *306*, 184–189. [CrossRef]